photonics

MDPI

Communication

Optical Chaos in Saturated Nonlinear Media

Fuqiang Li, Ziyang Chen, Jie Song, Meng Li and Cibo Lou *

College of Physical Science and Technology, Ningbo University, Ningbo 315211, China; 18394453438@163.com (F.L.); 23b311002@stu.hit.edu.cn (Z.C.); 13303534417@163.com (J.S.); limeng03121999@163.com (M.L.)
* Correspondence: loucibo@nbu.edu.cn

Abstract: In the study of the evolution of Gaussian beam in saturated nonlinear media, it is found that the probability of optical rogue waves changes with the change of nonlinearity. The light intensity distribution on the exit surface of nonlinear medium can be characterized by scintillation index, and the change of rogue wave corresponds to the evolution of scintillation index. The rogue wave probability shows a complex trend with the evolution of nonlinearity. The Lyapunov exponent and power spectrum method are used to determine that the probability of rogue wave is chaotic with nonlinear evolution.

Keywords: nonlinearity; rogue wave; chaos; lyapunov exponent; power spectrum

1. Introduction

Chaos has always been a research hotspot. Chaos exists in all nonlinear systems, including optics [1–3], atmospheric science [4], finance [5], and celestial systems [6]. In the optical nonlinear system, the early studies of optical chaos are mainly related to the unstable output of the laser. In recent studies, it was found that chaos can be observed through the collision of multiple objects. By means of theoretical and experimental studies on the propogation of wave function in a medium [7–11], it has been discovered that a unique optical phenomenon, known as optical soliton [12], is produced when there is a balance between the diffraction and self-focusing of a Gaussian beam. According to numerical study, the solitons of the GrossPitaevskii equation or the Lorenz–Haken equation exhibit chaos after a three-soliton collision [13]. In a recent study, Xin experimentally observed optical chaos after collisions of three solitons in a saturated nonlinear medium [14]. It has been proved numerically and experimentally that the collision of three or more solitons will produce optical chaos [13]. Another soliton collision discovered that multiple soliton which possess a specific level of energy and quantity collisions are often accompanied by the generation of Rogue waves (RWs) [15,16].

In a recent study, Avigliano found that in photorefractiveally saturated nonlinear media under appropriate nonlinear conditions, the nonlinear evolution of a tightly focused Gaussian beam (Gb) exhibits a RW probability distribution, and this probability increases with the increase of the external electric field. This study shows that as the nonlinearity increases, the tightly focused Gb with perturbation splits into filaments, which collide with each other [17]. In the same year, Chen found that under appropriate nonlinear conditions in saturated nonlinear media, the nonlinear evolution of a wide Gb also exhibits the distribution of RW probability [18]. It is certain that the collision of the filaments generated after the splitting of the Gb can also produce RWs. Since the probability of RWs generated by filament collision is irregular with the evolution of nonlinearity, this has attracted our attention [15].

The modulation of nonlinear propagation of Gb in saturated nonlinear media is related to the applied voltage and beam intensity. In this work, we set a fixed beam intensity and change the applied voltage to change the nonlinearity.

Citation: Li, F.; Chen, Z.; Song, J.; Li, M.; Lou, C. Optical Chaos in Saturated Nonlinear Media. *Photonics* **2023**, *10*, 600. https://doi.org/10.3390/photonics10050600

Received: 19 April 2023
Revised: 15 May 2023
Accepted: 19 May 2023
Published: 22 May 2023

In this work, we investigated the nonlinear evolution of RWs induced by a Gb with perturbation in a saturated nonlinear medium. We used the Lyapunov exponent [19–21] and power spectrum method [22–24] to study the existence of optical chaos through experiments and numerical simulations.

2. Experimental Setup

As shown in Figure 1, we used an SBN crystal with a cross-sectional area of 5×5 mm^2 and a length of 10 mm (propagation coordinate z). The saturation nonlinearity is adjusted by adjusting the applied voltage along the optical axis of the crystal. The incident light is a 532 nm wavelength laser with extraordinary polarization in the direction of the applied voltage. The beam width at half maximum is about 30 µm, and the input power is about 120 µW. A CCD camera is used to record the light intensity distribution profile at the input and output of the crystal.

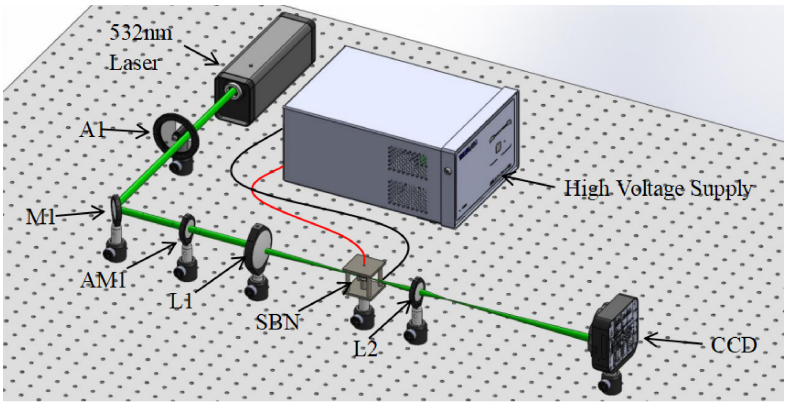

Figure 1. Experimental setup for observing the chaos. Here A1 is an attenuator, AM1 is a lens with a mask, M1 is a mirror, and L1 and L2 are lenses.

The applied voltage was varied to observe and collect the intensity distribution after the nonlinear modulation was stabilized. The voltage was increased from 0 V to 900 V with a step size of 15 V. In order to perform RW statistics, the experiment was repeated 100 times under each voltage. When the applied voltage is 0 V, the spot size on the output surface of the saturated nonlinear crystal is 42 µm, which is larger than the input profile due to linear diffraction. The input light propagates along the z-axis, and it has a non-uniform Gb with a large amount of perturbation, which is about 1% of the light intensity. The perturbation in the Gb is provided by an intensity mask AM1. These perturbations are important for splitting in the presence of nonlinearity.

Figure 2 shows the output beam profiles at various applied voltages. It can be seen that as nonlinearity increases, the perturbation in the incident light is gradually amplified in the propagation process, and the intensity distribution of the rear surface of the crystal shows a complex trend.

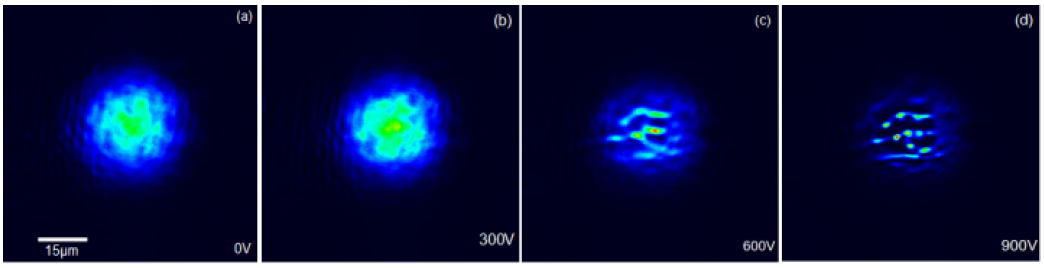

Figure 2. (**a**–**d**) are the light intensity distribution of the exit surface of the saturated nonlinear medium under the applied voltage of 0 V, 300 V, 600 V, 900 V, respectively.

Statistical analysis of RWs was conducted on the experimental data. Statistics follow the following principles: to determine the probability of RWs, the event with the anomaly index $AI = I/Ie > 2$ is regarded as RW. I is the intensity of each wave, and Ie is defined as the average value of the highest intensity tertile of the corresponding probability density function (PDF) distribution.

As shown in Figure 3, the long tail distribution can be clearly observed by counting 100 sets of data at 510 V in the experiment.

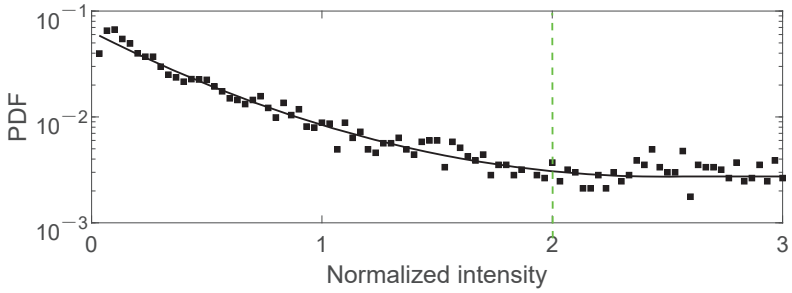

Figure 3. Strength statistics to minus sign. at 510 V. The vertical green dotted lines indicate the rogue waves (RW) thresholds.

The rogue wave probability under applied voltage is represented by P. We conduct rogue wave statistical analysis on the exit surface at different voltages using a total of 100 sets of experimental data [see Figure 4].

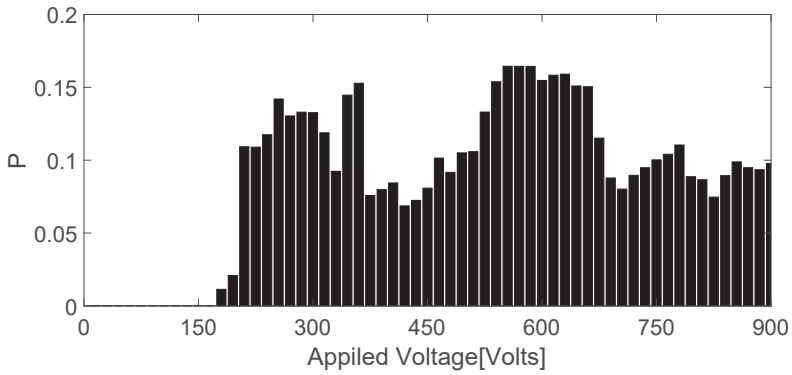

Figure 4. RWs probability as a function of the applied voltage.

We used scintillation index to describe the intensity distribution [25]. The scintillation index (Sz), which describes the average intensity gap of each filament is given as: $Sz = (|I^2| - |I|^2)/|I|^2$, where $|I^2|$ is the average of the square of light intensity of each filament on the exit plane and $|I|^2$ is the square of the average light intensity of each filament. At the same voltage, 100 sets of experimental data were collected repeatedly, and the scintillation index was calculated as shown in Figure 5.

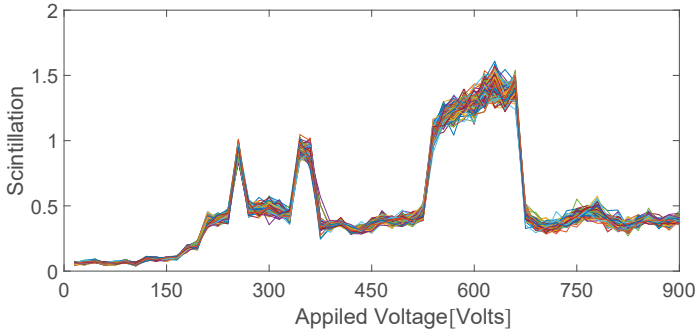

Figure 5. The scintillation index calculated from 100 sets of data.

We averaged 100 groups of scintillation indexes. The results are shown in Figure 6.

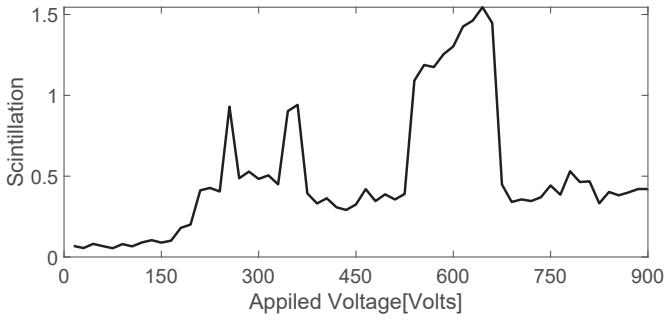

Figure 6. The average scintillation index calculated from 100 sets of experimental data.

When the scintillation index is compared to the RWs probability, it is clear that the two have the same evolution trend. By calculating the scintillation index and the probability of RWs, it can be analyzed that the scintillation index will increase when there is a strong spot. Similarly, the RW is a strong spot. The evolution of RWs probability with nonlinearity can be studied by studying the scintillation index.

We changed the incident light intensity to 99.5% of the previous level using the A1 device, then collected the light intensity distribution on the rear surface by repeating the previous experimental steps, and calculated the scintillation index. The scintillation index as a function of applied voltage obtained from the two experiments is shown in Figure 7.

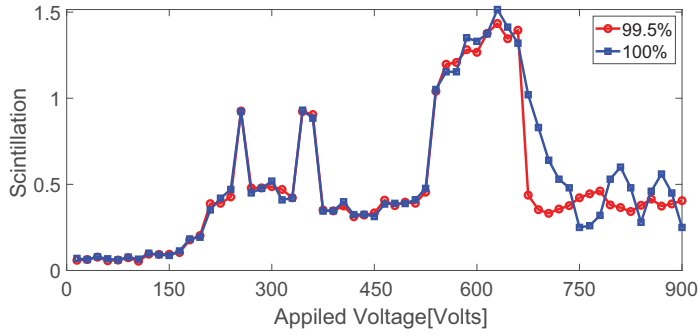

Figure 7. The scintillation index of the exit surface as a function of the applied voltage. Here 100% means no intensity attenuation, and 99.5% means 0.5% intensity attenuation.

It can be seen, as the light intensity changed by 0.5%, the evolution of the scintillation index is very intense and unpredictable in the later stage of nonlinear change, which is chaos.

Chaos is defined as a type of quasi-random motion with a specific location. The evolution process of a chaotic system is very sensitive to the initial conditions. We calculated the Lyapunov exponent (LE) to determine whether the evolution is chaotic [21]. LE can be calculated as [26]:

$$LE = \frac{1}{N} log \frac{\Delta(x_n)}{\Delta(x_0)} = \frac{1}{N} log \left| \frac{df^n(x_0)}{dx} \right| \quad (1)$$

where N is the length of the Scintillation index series, x_n is the scintillation index, x_0 is the scintillation index of 0 V. LE can be divided into three types: when $LE < 0$, the system converges to a fixed value; when $LE = 0$, the system is in a stable state; when $LE > 0$, the system diverges. The experimental data were reconstructed in phase space, and the time delay [27] and embedding dimension [28] were obtained by autocorrelation and false nearest neighbor methods, respectively. The calculation results are shown in Figure 8a,b.

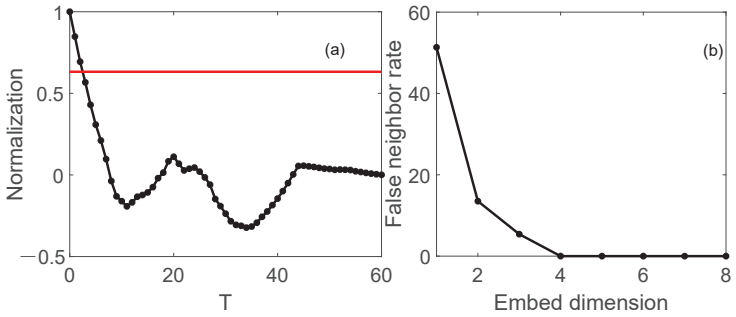

Figure 8. (**a**) The autocorrelation method was used to obtain the time delay, and the T corresponding to the intersection of the red line and the autocorrelation function line is the best time delay. (**b**) The embedding dimension was obtained by the false neighbor method. When the false neighbor rate is equal to 0, the corresponding embedding dimension is needed to reconstruct the phase space.

The calculated time delay is represented by T, $T = 3$, and the calculated embedding dimension is represented by m, $m = 4$.

We calculated the largest Lyapunov exponent and obtain the result is 0.19. The results are shown in Figure 9. The result of the largest Lyapunov index is greater than 0. Therefore, the RWs probability is chaotic with the evolution of the applied voltage.

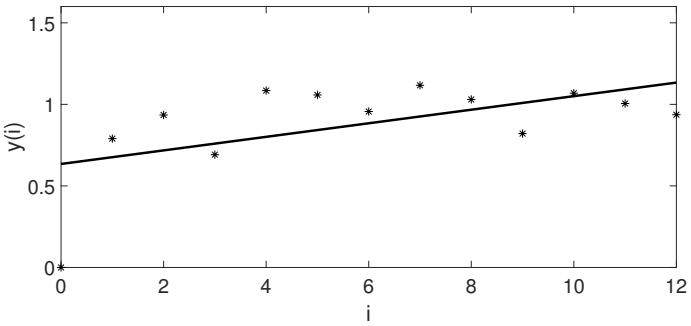

Figure 9. The Lyapunov exponent in the phase space of experimental data. * denotes the distance y (i) corresponding to each i.

For the chaotic evolution of the light intensity distribution of the SBN crystal exit surface with the increase of voltage, we verify our results from the perspective of the power spectrum. The power spectrum is the corresponding spatial spectrum in the process of system evolution. The power spectrum of periodic motion is discrete, with only a few peaks at different frequencies. White noise is due to the completely random motion, and its power spectrum has no continuous broad peak. Chaos is a local quasi-random system with the characteristics of periodic motion and complete random motion. Its power spectrum should have broad peaks and continuous low-intensity sub-peaks [22]. The scintillation index image of Figure 6 is converted into the power spectrum. The calculation method is as follows:

$$X(\omega) = \sum_{n=0}^{N-1} x(n) e^{-i\omega n} \tag{2}$$

$$S(\omega) = \frac{1}{N} |X(\omega)|^2 \tag{3}$$

where $x(n)$ is the scintillation index series, N is the length of the Scintillation index series, and $S(w)$ is the power spectrum. In this paper, we use the nonlinear power spectrum.

Figure 10 shows the experimentally measured power spectrum of the scintillation index. A high-power main peak and several low-power secondary peaks can be seen. Therefore, it can be concluded that in a saturated nonlinear medium, the evolution of the RWs generated by a Gb under appropriate nonlinearity is chaotic.

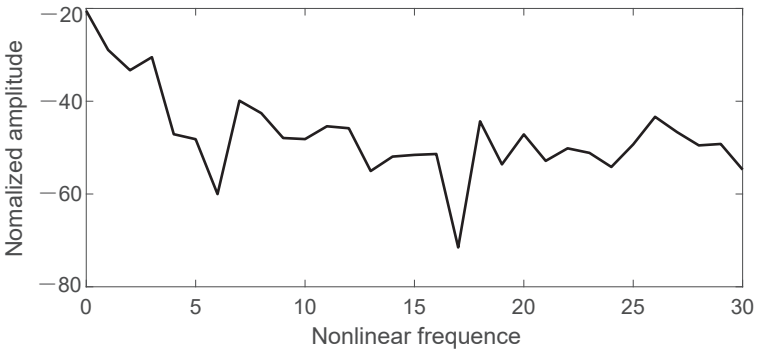

Figure 10. Power spectrum of scintillation index measured experimentally.

3. Numerical Simulation

To verify the experimental findings, we numerically simulate the chaotic phenomena on SBN crystal and compare them with the experimental results. The distributed beam propagation method (BPM) is used for numerical simulation. The propagation of Gb in SBN crystal satisfies the nonlinear Schrodinger equation [29]:

$$i\frac{\partial}{\partial(z)}\psi(x,y,z)+\frac{1}{2k_0}\bigtriangledown_{\perp}^{2}\psi(x,y,z)=-\Delta n\frac{k_0}{n_e}\psi(x,y,z) \tag{4}$$

where $\bigtriangledown_{\perp}^{2}$ is the Laplacian operator, z is the propagation distance, $\psi(x,y,z)$ is the slowly varying light wave envelope, $k_0=2\pi/\lambda$ is the wave vector, where λ is the wavelength of light, n_e is the refractive index of the extraordinary polarized beam in the SBN crystal. The change in refractive index Δn caused by the beam in SBN crystal can be given as:

$$\Delta n=\frac{1}{2}n_e^3\gamma_{33}E \tag{5}$$

where γ_{33} is the electro-optic coefficient. E can be expressed as:

$$E=E_0\frac{I_d}{I+I_d}-\frac{K_BT}{e}\frac{1}{I+I_d}\frac{\partial I}{\partial x} \tag{6}$$

where I is the intensity of light irradiation, I_d is the intensity of dark irradiation, E_0 is the external electric field, K_BT is the product of Boltzmann constant and absolute temperature, and e is the electron charge.

The full width at half maximum of the incident Gb was set equal to 30 µm, respectively. By adding a noise seed to the incident light to simulate the perturbation in the incident light, the noise intensity is set to 2% the amplitude of the incident light at the corresponding position. The lateral width of the crystal is 5 mm and the propagation length is 10 mm, with a refractive index n_e of 2.33 and an electro-optic coefficient of 280 pm/V. The rule to change the applied voltage for adjusting saturation nonlinearity is as follows: increase the voltage from 0 V to 900 V with a step of 15 V.

Before the RWs statistics, taking the RWs statistics under 800 V voltage as an example. At an applied voltage of 800 V, we repeated the simulation for 100 times, and performed probability statistics on all the spots obtained. We found that there was an obvious long-tail distribution as shown in Figure 11.

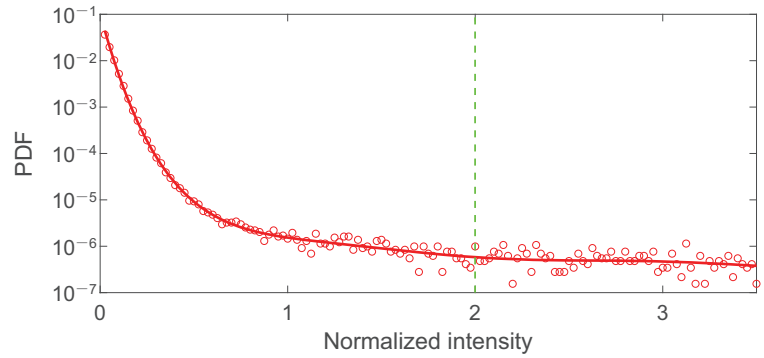

Figure 11. Numerical simulation of strength statistics at 800 V voltage. The vertical green dotted lines indicate the RWs thresholds.

At each voltage, we repeat the numerical simulation 100 times and count the Rw probability. The results are shown in Figure 12.

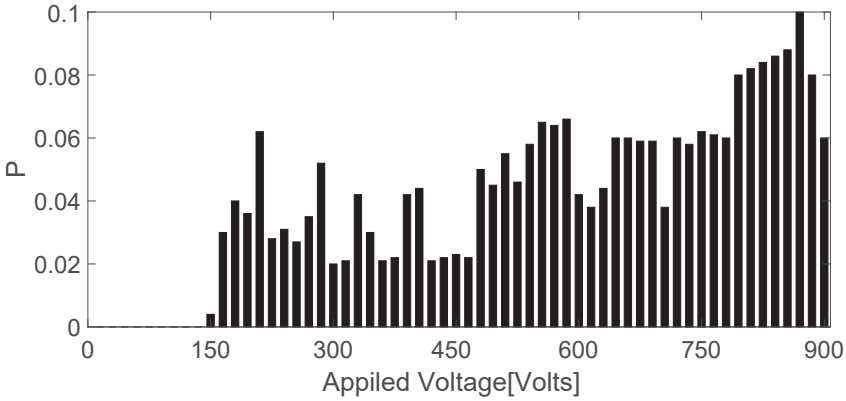

Figure 12. Simulated statistical probability of Plane RWs as a function of applied voltages.

After counting the probability of RWs, the scintillation index is calculated for the exit surface under different voltages. Under different voltages, the statistical scintillation index of the light intensity distribution of 100 groups of exit surfaces is shown in Figure 13. We averaged 100 groups of scintillation indexes, and the results are shown in Figure 14. As shown in Figures 12 and 14, the evolution trend of RWs probability and scintillation index is almost identical.

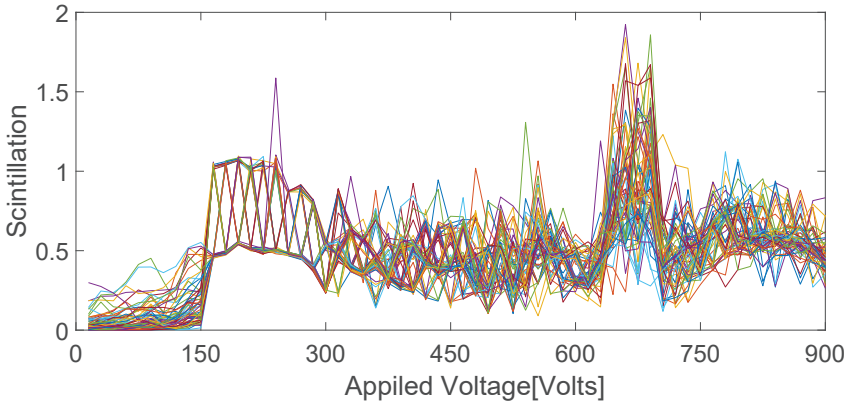

Figure 13. The scintillation index calculated by numerical simulation of 100 sets of data.

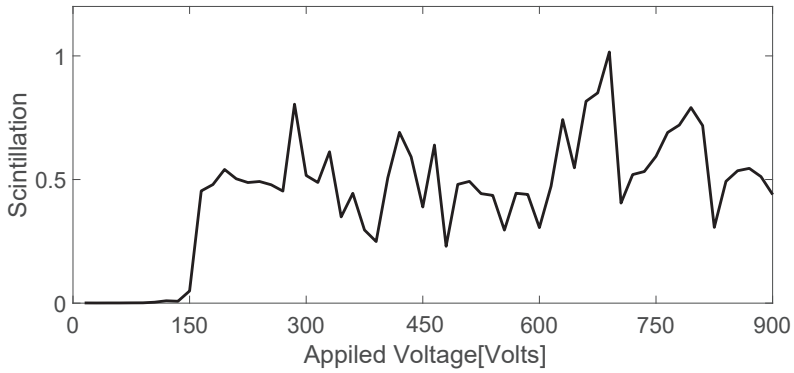

Figure 14. Numerical simulation of the scintillation index at the exit surface versus applied voltage.

To check if the evolution of the scintillation index is sensitive to the initial condition, we reduced the incident light intensity by 0.5%, and then repeated the above-described numerical simulation process. The results are shown in Figure 15.

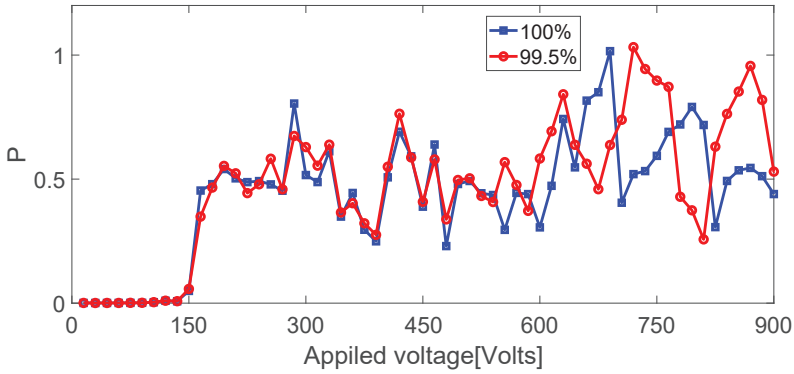

Figure 15. Numerical simulation of the scintillation index at the exit surface versus applied voltage. Here 100% means no intensity attenuation and 99.5% means 0.5% intensity attenuation.

Similarly, phase space reconstruction is performed on the simulated data. As shown in Figure 16, the time delay and embedding dimension are calculated by autocorrelation method and false nearest neighbor method. We calculate $T = 2$, $m = 4$.

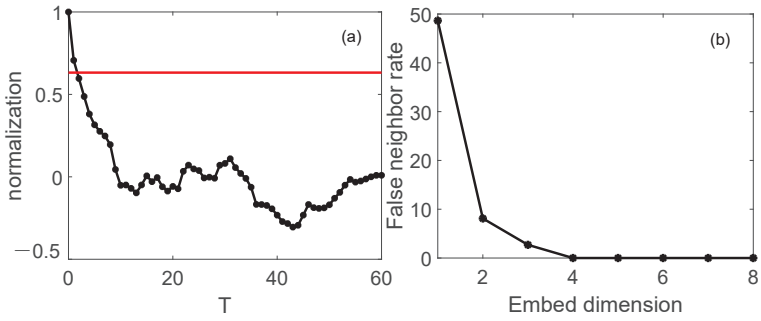

Figure 16. (**a**) The optimal time delay is obtained by autocorrelation method for numerical simulation data. (**b**) The embedding dimension of the simulated data is obtained by the false nearest neighbor method.

The Lyapunov exponent was calculated by phase space reconstruction of the simulated data. As shown in Figure 17, the calculated maximum Lyapunov exponent is 0.21. The maximum Lyapunov exponent is positive, so the evolution of the RWs probability with nonlinearity is chaotic.

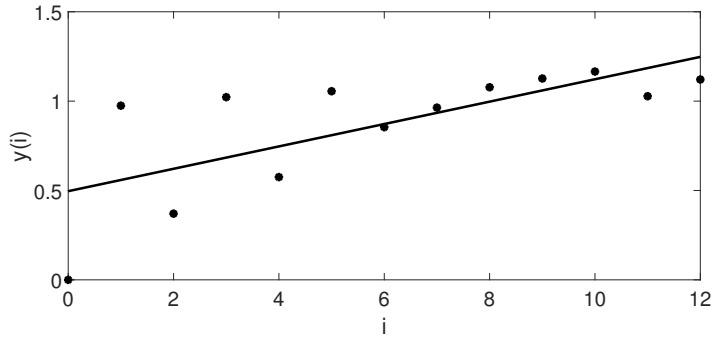

Figure 17. The Lyapunov exponent calculated by the simulated data phase space.

We also used the power spectrum method to verify the above results. The obtained results are shown in Figure 18. The power spectrum had the characteristics of wide peak and continuous sub-peak, which accorded with the power spectrum characteristics of chaos.

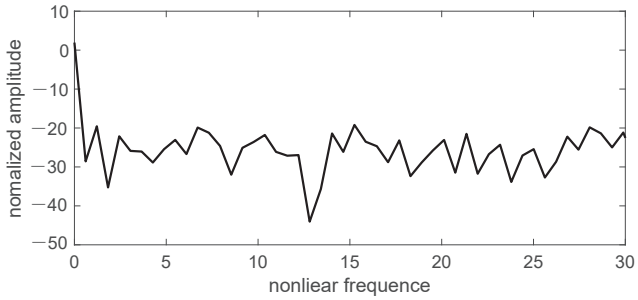

Figure 18. Numerically simulated scintillation index power spectrum.

The simulation shows that as the voltage increases, RWs probability becomes chaotic.

4. Conclusions

Through statistical experiments and numerical simulations, Gaussian beams exhibit filamentation caused by modulation instability in saturated nonlinear crystals. The collision of spots after splitting is the main reason for the generation of RWs. In previous studies, the evolution of RWs probability with nonlinearity was not studied. The light intensity distribution of the exit surface is characterized by the scintillation index, and it is found that the scintillation index and the RWs probability are consistent with the trend of nonlinear evolution. It is proved by the Lyapunov exponent greater than 0 and the power spectrum with wide peak and continuous sub-peak characteristics that with the increase of nonlinearity, the probability of obtaining RWs is chaotic. In the following work, we will study the time evolution of Gb in SBN crystals under giant nonlinearity and the relationship between optical RWs and optical chaos.

Author Contributions: Methodology, F.L. and C.L.; software, F.L., J.S., M.L. and Z.C.; validation, F.L.; writing original draft: F.L.; writing—review & editing, F.L.; project administration, C.L.; funding acquisition, C.L. All authors have read and agreed to the published version of the manuscript.

Funding: This research was funded by National Natural Science Foundation of China (12074207).

Institutional Review Board Statement: Not applicable.

Informed Consent Statement: Not applicable.

Data Availability Statement: Data underlying the results presented in this paper are not publicly available at this time but may be obtained from the authors upon reasonable request.

Acknowledgments: Thank Hu Yi for his helpful discussion.

Conflicts of Interest: The authors declare no conflict of interest.

References

1. Haken, H. Analogy between higher instabilities in fluids and lasers. *Phys. Lett. A* **1975**, *53*, 77–78. [CrossRef]
2. Gibbs, H.M.; Hopf, F.A.; Kaplan, D.L.; Shoemaker, R.L. Observation of chaos in optical bistability. *Phys. Rev. Lett.* **1981**, *46*, 474. [CrossRef]
3. Weiss, C.O.; Klische, W.; Ering, P.S.; Cooper, M. Instabilities and chaos of a single mode NH_3 ring laser. *Opt. Commun.* **1985**, *52*, 405–408. [CrossRef]
4. Lorenz, E.N. Deterministic nonperiodic flow. *J. Atmos. Sci.* **1963**, *20*, 130–141. [CrossRef]
5. Wang, Z.; Huang, X.; Shi, G. Analysis of nonlinear dynamics and chaos in a fractional order financial system with time delay. *Comput. Math. Appl.* **2011**, *62*, 1531–1539. [CrossRef]
6. Crawford, J.D. Introduction to bifurcation theory. *Rev. Mod. Phys.* **1991**, *63*, 991. [CrossRef]
7. Huang, Z.; Zhu, W.; Feng, Y.; Deng, D. Spatiotemporal self-accelerating Airy–Hermite–Gaussian and Airy–helical–Hermite–Gaussian wave packets in strongly nonlocal nonlinear media. *Opt. Commun.* **2019**, *441*, 195–207. [CrossRef]
8. Rodrigues Gonçalves, M.; Rozenman, G.G.; Zimmermann, M.; Efremov, M.A.; Case, W.B.; Arie, A.; Shemer, L.; Schleich, W.P. Bright and dark diffractive focusing. *Appl. Phys. B* **2022**, *128*, 51. [CrossRef]
9. Rozenman, G.G.; Schleich, W.P.; Shemer, L.; Arie, A. Periodic wave trains in nonlinear media: Talbot revivals, Akhmediev breathers, and asymmetry breaking. *Phys. Rev. Lett.* **2022**, *128*, 214101. [CrossRef]
10. Rozenman, G.G.; Shemer, L.; Arie, A. Observation of accelerating solitary wavepackets. *Phys. Rev. E* **2020**, *101*, 050201. [CrossRef]
11. Chen, Y.; Hosseini, B.; Owhadi, H.; Stuart, A.M. Solving and learning nonlinear PDEs with Gaussian processes. *J. Comput. Phys.* **2021**, *447*, 110668. [CrossRef]
12. Gupta, N. Multi Gaussian Breather Solitons in Diffraction Managed Nonlinear Optical Media. *Nonlinear Opt. Quantum Opt. Concepts Mod. Opt.* **2022**, *55*, 309–330.
13. Dalfovo, F.; Giorgini, S.; Pitaevskii, L.P.; Stringari, S. Theory of Bose-Einstein condensation in trapped gases. *Rev. Mod. Phys.* **1999**, *71*, 463. [CrossRef]
14. Xin, F.; Di Mei, F.; Falsi, L.; Pierangeli, D.; Conti, C.; Agranat, A.J.; DelRe, E. Evidence of chaotic dynamics in three-soliton collisions. *Phys. Rev. Lett.* **2021**, *127*, 133901. [CrossRef]
15. Eberhard, M.; Savojardo, A.; Maruta, A.; Römer, R.A. Rogue wave generation by inelastic quasi-soliton collisions in optical fibres. *Opt. Express* **2017**, *25*, 28086–28099. [CrossRef]
16. Peng, J.; Tarasov, N.; Sugavanam, S.; Churkin, D. Rogue waves generation via nonlinear soliton collision in multiple-soliton state of a mode-locked fiber laser. *Opt. Express* **2016**, *24*, 21256–21263. [CrossRef]
17. Hermann-Avigliano, C.; Salinas, I.A.; Rivas, D.A.; Real, B.; Mančić, A.; Mejía-Cortés, C.; Maluckov, A.; Vicencio, R.A. Spatial rogue waves in photorefractive SBN crystals. *Opt. Lett.* **2019**, *44*, 2807–2810. [CrossRef]
18. Chen, Z.; Li, F.; Lou, C. Statistical study on rogue waves in Gaussian light field in saturated nonlinear media. *Chin. Opt. Lett.* **2022**, *20*, 081901. [CrossRef]
19. Rosenstein, M.T.; Collins, J.J.; De Luca, C.J. A practical method for calculating largest Lyapunov exponents from small data sets. *Phys. D Nonlinear Phenom.* **1993**, *65*, 117–134. [CrossRef]
20. Wolf, A.; Swift, J.B.; Swinney, H.L.; Vastano, J.A. Determining Lyapunov exponents from a time series. *Phys. D Nonlinear Phenom.* **1985**, *16*, 285–317. [CrossRef]
21. Cheng, S.; Chen, H.; Qing, T. Nonlinear dynamics of slider crank mechanism with rubber linkage. *J. Mech. Electr. Gineering* **2020**, *37*, 607–613.
22. Lyapunov, A.M. The general problem of the stability of motion. *Int. J. Control* **1992**, *55*, 531–534. [CrossRef]
23. Murakami, A.; Shore, K. Mean spectral phase and detection of masked periodic signals in chaotic carriers. *IET Optoelectron.* **2011**, *5*, 114–120. [CrossRef]
24. Allio, R.; Guzmán-Silva, D.; Cantillano, C.; Morales-Inostroza, L.; Lopez-Gonzalez, D.; Etcheverry, S.; Vicencio, R.A.; Armijo, J. Photorefractive writing and probing of anisotropic linear and nonlinear lattices. *J. Opt.* **2015**, *17*, 025101. [CrossRef]
25. Qian, X.-M.; Zhu, W.-Y.; Rao, R.-Z. Long-distance propagation of pseudo-partially coherent Gaussian Schell-model beams in atmospheric turbulence. *Chin. Phys. B* **2012**, *21*, 094202. [CrossRef]
26. Baozhou, L. Research on Power Spectrum Estimation and Improved Algorithm of Periodic Graph Method. *Electron. Meas. Technol.* **2020**, *43*, 76–79.
27. Kantz, H.; Schreiber, T. *Nonlinear Time Series Analysis*; Cambridge University Press: Cambridge, UK, 2004.
28. Cedeño González, J.R.; Flores, J.J.; Fuerte-Esquivel, C.R.; Moreno-Alcaide, B.A. Nearest neighbors time series forecaster based on phase space reconstruction for short-term load forecasting. *Energies* **2020**, *13*, 5309. [CrossRef]
29. Deeming, T.J. Fourier analysis with unequally-spaced data. *Astrophys. Space Sci.* **1975**, *36*, 137–158. [CrossRef]